Scripta Materialia 185 (2020) 30–35

Contents lists available at ScienceDirect

Scripta Materialia

journal homepage: www.elsevier.com/locate/scriptamat

Characterization at high spatial and angular resolutions of deformed nanostructures by on-axis HR-TKD

Clément Ernould[a,b], Benoît Beausir[a,b], Jean-Jacques Fundenberger[a,b], Vincent Taupin[a,b], Emmanuel Bouzy[a,b,*]

[a] Université de Lorraine, CNRS, LEM3, F-57000 Metz, France
[b] Laboratory of Excellence on Design of Alloy Metals for low-mAss Structures (DAMAS), University of Lorraine, 57073 Metz, France

ARTICLE INFO

Article history:
Received 18 December 2019
Revised 30 March 2020
Accepted 3 April 2020

Keywords:
On-axis Transmission Kikuchi Diffraction (TKD)
HR-TKD
Nanostructured materials
Severe Plastic Deformation (SPD)
Electron diffraction

ABSTRACT

Global Digital Image Correlation (DIC) is applied on the electron diffraction patterns acquired by the "on-axis" Transmission Kikuchi Diffraction (TKD) technique. High-angular resolution (HR-TKD) mappings of the grain internal disorientations and the associated geometrically necessary dislocation densities are then derived at a nanoscale resolution. Tailored for the fine characterization of nanomaterials in the scanning electron microscope (SEM), the method is illustrated on a nanostructured high-purity aluminium processed by severe plastic deformation (SPD) and its performances are discussed in the light of imaging by transmission electron microscopy (TEM) and by SEM using a forescatter electron detector (FSD).

As compared to coarse grain polycrystalline materials, nanostructured metallic materials (NMM) show outstanding mechanical properties such as superior strength. This stems from their extreme grain refinement as obtained for instance by high energy ball milling [1] or by severe plastic deformation (SPD) [2]. In order to understand the plastic deformation mechanisms and the grain fragmentation processes [3] leading to such microstructures, crystallographic orientations are commonly investigated by means of electron diffraction techniques. In the scanning electron microscope (SEM), assessing grain internal disorientations and geometrically necessary dislocation (GND) densities at both high spatial and angular resolutions remains a challenging task, which the present article addresses in the case of aluminium deformed by equal channel angular extrusion (ECAE).

As a first challenge, a nanoscale spatial resolution is required. The common Electron backscattered diffraction (EBSD) technique has an effective lateral resolution of about 50 nm [4]. Characterizing nanocrystalline materials is only possible in heavy elements such as platinum [5]. To overcome such limitations, Keller and Geiss [6] introduced the Transmission Kikuchi Diffraction (TKD) technique in 2012 where a 50-150 nm thin foil is observed in transmission in the SEM. Reaching spatial resolutions between 3 and 10 nm [6,7], which is not far from the one nanometre achievable in Transmission electron Microscopy (TEM) [8], TKD was first applied to NMM by Trimby et al. [9]. In 2015, Fundenberger et al. [10,11] proposed an "on-axis" configuration where the scintillator is placed beneath the specimen, perpendicularly to the electron beam. It results in faster acquisition times, in a lower pattern distortion [12,13] and in a slightly better lateral spatial resolution [13,14] than the "off-axis" one. Regarding the depth resolution of TKD orientation mapping, it varies in opposite ways with incident energy [15,16]. It is about a few tens of nanometres [7,16] while the diffraction signal in TEM originates from the whole sample thickness, which may contain several grains.

As a second challenge, the angular resolution should be as accurate as possible to follow the structural evolution during early grain fragmentation processes. SEM-based techniques standardly use the Hough transform-based indexation (HTI) [17] which determines crystallographic orientations with a precision around 0.5°. New techniques are emerging, namely the dictionary [18] and the spherical harmonic transform [19,20] based approaches, having an improved noise robustness and an accuracy of 0.1-0.2°. Regarding TEM, orientations are determined either from Kikuchi lines [21,22] or from diffraction spots using the Precession Electron Diffraction Automated Crystal Orientation Mapping (PED-ACOM)

* Corresponding author at: Laboratoire d'Etude des Microstructures et de Mécanique des Matériaux (LEM3, UMR CNRS 7239), Université de Lorraine, 7 rue Félix Savart - 57070 METZ, France.
E-mail address: emmanuel.bouzy@univ-lorraine.fr (E. Bouzy).

https://doi.org/10.1016/j.scriptamat.2020.04.005
1359-6462/

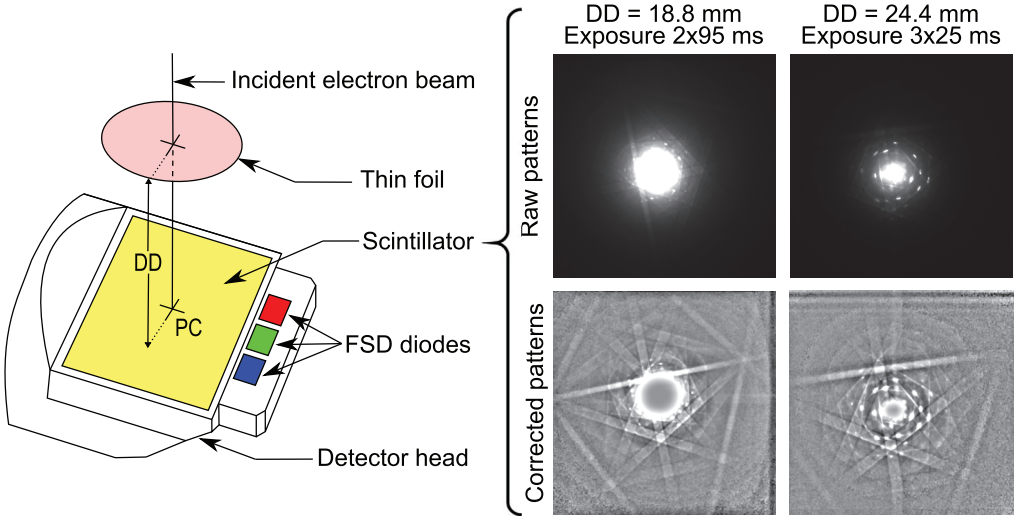

Fig. 1. (left) Scheme of the "on-axis" TKD detector head which includes a forescatter electron detector (FSD) and a scintillator. The projection geometry is defined by the sample-to-detector distance (DD) and the position of the pattern centre (PC). (right) EDP before and after background correction. Both patterns are acquired approximately at the same location using the two sets of acquisition parameters summed up in Table 1. (For interpretation of the references to colour in this figure legend, the reader is referred to the web version of this article.)

technique [23] with typical angular resolutions of 0.3° [24] and 0.8-1.1° [8,24], respectively. Refinement algorithms accounting for the spot intensities enables to close this gap [25].

Disorientation angles and GND densities deduced from both SEM and TEM orientation mappings [26,27] are directly impacted by angular uncertainties, which are fateful at low disorientation angles (< 1°) [28]. For SEM-based techniques, lattice curvature and elastic strains are measured with an accuracy up to 10^{-4} [29] using high angular resolution EBSD (HR-EBSD) technique [30]. Basically, it uses digital image correlation (DIC) techniques to recover the displacement field between a reference and a target high-quality electron diffraction patterns (EDP). HR-EBSD is currently experiencing substantial developments in terms of pattern registration [31–35], SEM calibration [36] or determination of the absolute orientations [37] with recent applications to "off-axis" [38] and "on-axis" [35] TKD. Since the performances strongly depend on the pattern quality, most studies focus on single crystals or slightly deformed materials. Here, we further show that it has also a great potential for characterising strongly plastically deformed and fine grain polycrystalline materials.

To this end, the high-spatial resolution of the "on-axis" TKD technique is coupled with the high-angular resolution of the DIC (HR-TKD) to characterize, in terms of grain internal disorientations and GND densities, the nanostructure of a high purity aluminium as obtained after 10 passes of ECAE. Results are discussed in the light of a recent SEM imaging technique based on a forescatter electron detector (FSD) as well as TEM imaging.

A thin foil obtained by twin-jet electro-polishing is investigated using a Zeiss Supra 40 FEG-SEM. A Bruker e$^-$Flash HR+ camera is attached to a Bruker OPTIMUS detector for the on-axis TKD. The latter (scheme in Fig. 1) includes a FSD and an horizontal phosphor scintillator placed beneath the sample. Besides the Kikuchi diffraction signal, both detectors capture the incoherent background and the diffraction spots, which are not selective in depth. The FSD consequently images the entire sample thickness whereas only the non-absorbed Kikuchi signal stemming from the vicinity of the underside of the sample is considered to map the orientations by TKD. Note that the bands are barely visible in the absence of background correction in Fig. 1 due to the large dynamics in the intensities of the raw patterns caused by both spots and inelastic scattering.

Thanks to its three diodes, the FSD provides coloured images whose contrast varies in a very sensitive way and depends on many parameters such as the sample thickness, chemical composition or crystal orientation. Here, given that there is a single phase and considering the thickness relatively constant on the observed areas, the FSD image in Fig. 2a mainly displays an orientation contrast. The lateral resolution is also sufficient to observe dislocations as highlighted by the close-up in Fig. 2a'. Thus, FSD imaging allows to visualise the ECAE deformed structure in terms of intra-granular orientation changes and dislocation arrangements. The microstructure is composed of elongated, 50-200 nm thick grains, characteristic of a microstructure strongly sheared after 10 passes of ECAE. GND walls form within the grains and reflect incompatibility of the heterogeneous deformation within grains. Thus, a substructure is formed inside the elongated grains leading to their fragmentation. Here, the subgrain boundaries are highlighted by the sudden colour changes of the FSD contrast in Fig. 2a', making the FSD image at some point easier to interpret than the TEM bright field image in Fig. 2d. FSD imaging remains nevertheless qualitative. Quantitative parameters, such as the fraction and nature of low angle grain boundaries (LAGB) or the GND densities, are required to better characterize grain fragmentation processes.

Complementary to FSD imaging, orientation mapping with both high spatial and high angular resolutions is paramount. Knowing the spatial arrangement of deformation structures thanks to the FSD in Fig. 2a, acquisition parameters for the TKD orientation mapping can be chosen accordingly, in particular the step size which is here of 6.5 nm. As indicated by the area delimited by a dotted-line in Fig. 2a, a second map is also realised at a magnification of 500,000. The latter aims at characterizing the striations appearing in the FSD image and will be discussed later. Table 1 sums up the experimental settings for both mappings, for which 600×600 px^2 (2×2 binning) EDP with a 16-bits grayscale are recorded for the DIC analysis to be performed later on. The latter analysis uses the SEM calibration provided by the indexing software.

The grain internal disorientations in Fig. 2b are derived from the crystallographic orientations as determined by the Bruker's ESPRIT 1.9 software, where the resolution of the HTI is set to its maximum. Within each grain, the local disorientation angles are measured with respect to a reference point denoted by a white cross in Fig. 2b. The latter is associated to the reference pattern

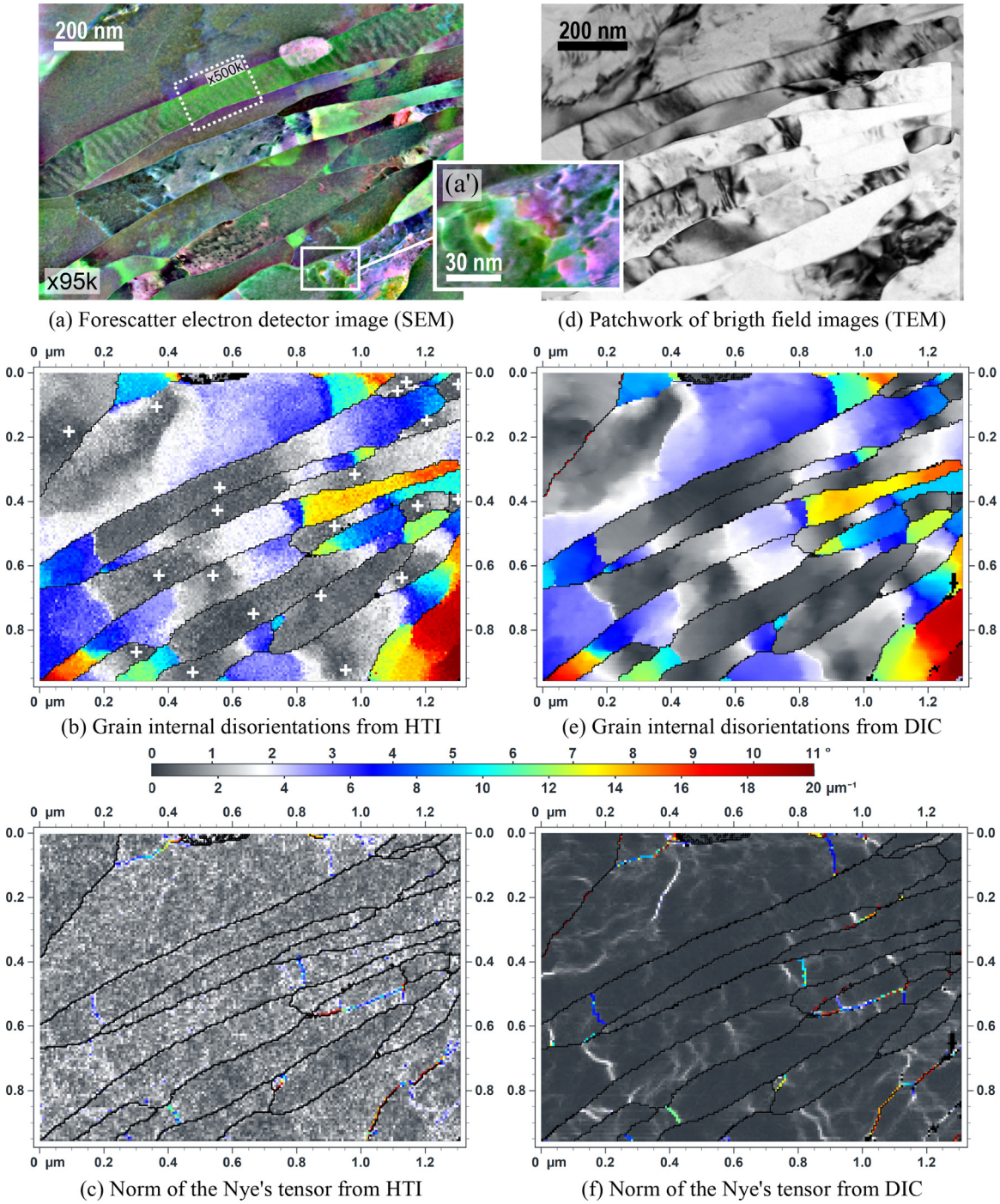

Fig. 2. (a) FSD image of pure aluminium after 10 passes of ECAE observed at a magnification of × 95,000 with a probe current of 0.13 nA. Grain internal disorientations and norm of the Nye's dislocation tensor deduced from the Hough-transform based indexation (b and c respectively) and from DIC (e and f respectively). (d) Bright field image using a TEM. The latter is actually a patchwork of three images acquired with different tilts. (For interpretation of the references to colour in this figure legend, the reader is referred to the web version of this article.)

Table 1
SEM settings for data acquisition.

Magnification	Voltage [keV]	Current [nA]	Working distance / Detector distance [mm]	Step size [nm]	Exposure [ms] / Averaging
×95,000	30	1.25	6.9/18.8	6.5	95 ms / ×2
×500,000	30	1.25	2.5/24.4	3	25 ms / ×3

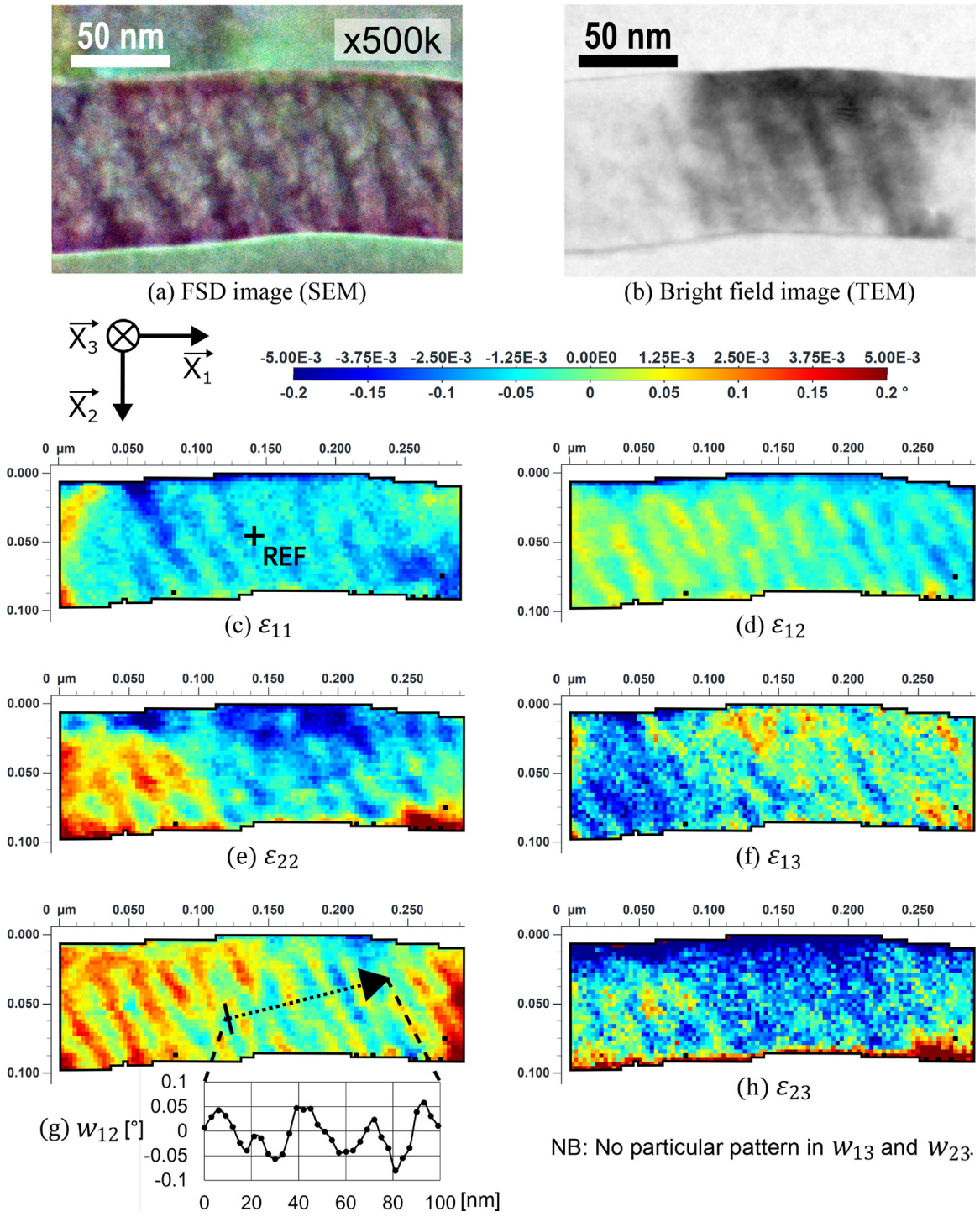

Fig. 3. (a) FSD observation of the striated grain within the region delimited by a dotted-line in Fig. 2a. (b) TEM observation of the same region. Note that it suffers from the contamination during the previous TKD mapping. (c)-(h) HR-TKD mappings of the deviatoric elastic strains ε_{11}, ε_{12} , ε_{13}, ε_{22}, ε_{23} and the rotation angle ω_{12} for which a line profile is plotted. The reference pattern is spotted by a black cross in (c).

considered during the subsequent DIC analysis. Domains disorientated up to 11° are present, while the orientations stay relatively constant within domains, consistently with the FSD contrast (Fig. 2a). In order to evidence the grain fragmentation, the GND densities are derived from the lattice curvature $\boldsymbol{\kappa}$, approximated with a finite difference scheme applied on the disorientations $\boldsymbol{\theta} = (\ \theta_1 \quad \theta_2 \quad \theta_3\ )^T$ as follows [27] (frame drawn in Fig. 3): $\kappa_{ij} \cong \Delta\theta_i/\Delta x_j$, where Δx_j is the step size of the orientation map in the direction x_j. By neglecting the elastic strains, which is a reasonable and usual assumption for the study of plastically deformed materials by means of HR-EBSD [39,40], the Nye's dislocation tensor $\boldsymbol{\alpha}$ [41] is obtained from $\boldsymbol{\alpha} \cong tr(\boldsymbol{\kappa}).\boldsymbol{I} - \boldsymbol{\kappa}^T$. Its entrywise norm $\boldsymbol{\alpha} = \sqrt{\alpha_{ij}.\alpha_{ij}}$ is shown with μm^{-1} units in Fig. 2c and Fig. 2f. It can be converted to m^{-2} by dividing it by the magnitude of the burgers vector b. Here, if b=0.286 nm, 1 μm^{-1} corresponds to $3.5 \times 10^{15}\ m^{-2}$.

In order to recover both disorientation angle and axis more accurately than the HTI method, a 'global' DIC analysis recently pro-

posed by the authors [35] and implemented in the ATEX-software [42] is conducted. This 'global' approach considers EDP as a whole through a large and unique region of interest (ROI). If its principle is similar with recent and independent works [31–33], the method stands out by its automated EDP pre-alignment based on Fourier-Mellin and Fourier transforms cross-correlation. This initial guess fairly accounts for the effects of rotations, enabling the analysis to deal with the large disorientations or orientation discontinuities present in the material analysed here. It also improves the computational efficiency of the subsequent inverse-compositional Gauss-Newton (IC-GN) algorithm [35]. Used for subpixel registration, the IC-GN algorithm iteratively measures the relative deformations between the target ROI and the reference, which are modelled by a first-order homography shape function. The SEM calibration parameters as well as their variations across the orientation map are only considered afterwards to analytically deduce the deviatoric elastic deformation gradient tensor from the DIC measurements. This constitutes another originality of the approach.

The signal-to-noise ratio is relatively low as compared to HR-EBSD standards, as shown by the reference EDP of the striated grain extracted from both datasets in Fig. 1. This is due to plastic deformation, which blurs EDP, in addition to the short exposure times set to prevent beam drift effects (see Table 1). Nevertheless, the accuracy on the internal disorientation angles and axis is significantly improved as compared to HTI method, as shown in Fig. 2e and f, respectively. The norm of the Nye's tensor derived from the DIC analysis and shown in Fig. 2f is revealing fine details, including GND walls and sharp subgrain boundaries. It also reveals some LAGB. Importantly, note that most of these details are missed by the HTI method, due to the uncertainty in the disorientation axis. Most of GND patterns are unclear or barely visible, and most of the dislocation structures are completely absent below $\sim 2^\circ$ of disorientation.

In order to investigate the striated grain, a FSD observation at a higher magnification of the area delimited by the dotted-line in Fig. 2a is performed and shown in Fig. 3a. The striations appear in the FSD image as an alternation of diffuse domains of about 25 nm width separated by narrower and darker regions, in which no dislocation is visible. TEM imaging in Fig. 3b leads to the same observations. Both imaging techniques suggest that only small elastic lattice rotations and/or strains are present. Now, both the SEM and the DIC are pushed to their limits by using a step size of 3 nm while shortening the exposure time and therefore the EDP quality. The DIC analysis indeed reveals the presence of elastic strains and rotations in Fig. 3c-h, while there is no GND density. Note that elastic strains are determined with respect to the reference pattern designated by the black cross in Fig. 3c. Consequently, they are relative to a material point that is not necessarily strain free. Due to the uncertainty on SEM calibration, these mappings are rather qualitative but nevertheless illustrate the high sensitivity of the technique. According to the in-plane rotation ω_{12} in Fig. 3g, the crystal alternatively switches from one orientation to the other, with a maximum amplitude of about 0.2°. Moreover, the line profile indicates that the angular resolution is better than 0.05°, enabling to observe variations undetectable by current indexation techniques.

To make high resolution mapping with steps of a few nanometres, it is preferable to use the on-axis TKD configuration rather than the off-axis TKD configuration. Indeed, the measurement time is much shorter which allows limiting the drift. In comparison with TEM-based techniques, the coupling of "on-axis" TKD orientation mapping with DIC and its association to FSD imaging to give a qualitative description and a quantitative analysis of deformation nanostructures, presents some advantages and a few drawbacks. The tri-colour code of the FSD imaging limits the ambiguous cases that can occur in grayscale images of TEM bright field, where a given grey intensity can correspond to different orientations. Moreover, dislocations can be visualized as in TEM, although the lateral spatial resolution is slightly larger. Regarding the orientation mapping, for TEM the spatial resolution is related to the electron beam size which can be as small as 0.5 nm with a field emission gun (FEG). For TKD, this resolution degrades to be around a few nanometres depending on the thickness of the sample. This is due to the larger beam broadening through the sample when working at lower electron energy in the SEM. However, this lower electron energy becomes an advantage concerning the depth resolution of TKD orientation mappings. Only a layer of a few tens of nanometres located at the outlet face of the incident beam contributes to the captured Kikuchi signal [16]. Thus, TKD is of valuable interest for the study of NMM where several grains can be contained in the sample thickness. Conversely, the non-selectivity in depth of the TEM techniques leads to superimposed patterns making orientation determination cumbersome [43]. Finally, the angular resolution of the TEM-based techniques is about 0.3° on orientation [24,25], which is comparable to that of the Hough-transform based indexation in the SEM-based techniques. As illustrated in this article, such an uncertainty deteriorates the sensitivity of the GND density measurement with the consequence that a part of the grain substructure information is missed. From this standpoint, DIC is applied to the EDP so that small disorientations of the order of 0.01-0.1° are captured. Note that TKD and HR-TKD are benefiting from the greatest sensitivity of the Kikuchi bands to the orientation as compared to diffraction spots. As pointed out by Leff et al. [44], a possible solution for the TEM-based techniques to improve the angular resolution would be to apply the DIC to the automated orientation mapping on Kikuchi patterns [22].

In conclusion, coupled with the DIC, the on-axis TKD technique enables a qualitative description and quantitative analysis of the deformed nanostructures.

- FSD imaging offers a fine and qualitative complementary observation of the deformation nanostructures, from which the acquisition parameters of the orientation mappings can then be chosen accordingly.
- Both high-spatial (3 nm) and high-angular ($<0.05^\circ$) resolutions are simultaneously achieved for the mapping of internal disorientations and the GND densities.
- Considering the material investigated here, i.e. nanocrystalline, plastically deformed, displaying large disorientation gradients and composed of a light element (aluminium), the technique should be easily applicable to a wider range of materials.

Acknowledgments

The authors thank Prof. László Tóth for providing the pure aluminium sample deformed by Equal Channel Angular Extrusion.

References

[1] J.S. Benjamin, MT 1 (1970) 2943–2951.
[2] Y. Estrin, A. Vinogradov, J. Microsc. 61 (2013) 782–817.
[3] Y. Cao, S. Ni, X. Liao, M. Song, Y. Zhu, Mater. Sci. and Eng. R Rep. 133 (2018) 1–59.
[4] R.A. Schwarzer, 2nd ed., Springer, US, 2009, pp. 1–20.
[5] D. Dingley, J. Microsc. 213 (2004) 214–224.
[6] R.R. Keller, R.H. Geiss, J. Microsc. 245 (2012) 245–251.
[7] R. van Bremen, D. Ribas Gomes, L.T.H. de Jeer, V. Ocelík, J.Th.M. De Hosson, Ultramicroscopy 160 (2016) 256–264.
[8] D. Viladot, M. Véron, M. Gemmi, F. Peiró, J. Portillo, S. Estradé, J. Mendoza, N. Llorca-Isern, S. Nicolopoulos, J. Microsc. 252 (2013) 23–34.
[9] P.W. Trimby, Ultramicroscopy 120 (2012) 16–24.
[10] J.-J. Fundenberger, E. Bouzy, D. Goran, J. Guyon, A. Morawiec, H. Yuan, Microsc. Microanal. 21 (2015) 1101–1102.
[11] J.J. Fundenberger, E. Bouzy, D. Goran, J. Guyon, H. Yuan, A. Morawiec, Ultramicroscopy 161 (2016) 17–22.
[12] H. Yuan, E. Brodu, C. Chen, E. Bouzy, J.-J. Fundenberger, L.S. Toth, J. Microsc. 267 (2017) 70–80.

[13] F. Niessen, A. Burrows, A.B da, S. Fanta, Ultramicroscopy 186 (2018) 158–170.
[14] Y. Shen, J. Xu, Y. Zhang, Y. Wang, J. Zhang, B. Yu, Y. Zeng, H. Miao, Appl. Sci. 9 (2019) 4478.
[15] E. Brodu, E. Bouzy, J.-.J. Fundenberger, Ultramicroscopy 181 (2017) 123–133.
[16] E. Brodu, E. Bouzy, Microsc. Microanal. 23 (2017) 1096–1106.
[17] N.C. Krieger Lassen, K. Conradsen, D. Juul Jensen, Scann. Microsc. 6 (1992) 115–121.
[18] Y.-.H. Chen, S.U. Park, D. Wei, G. Newstadt, M. Jackson, J.P. Simmons, M. De Graef, A.O. Hero, Phys. Stat. (2015).
[19] W.C. Lenthe, S. Singh, M.D. Graef, Ultramicroscopy 207 (2019) 112841.
[20] R. Hielscher, F. Bartel, T.B. Britton, Microsc. Microanal. 25 (2019) 1954–1955.
[21] S. Zaefferer, R.A. Schwarzer, Z. Metallkd. 85 (1994) 585–591.
[22] J.-.J. Fundenberger, A. Morawiec, E. Bouzy, J.S. Lecomte, Ultramicroscopy 96 (2003) 127–137.
[23] E.F. Rauch, M. Veron, Mater. Werkst. 36 (2005) 552–556.
[24] A. Morawiec, E. Bouzy, H. Paul, J.J. Fundenberger, Ultramicroscopy 136 (2014) 107–118.
[25] E.F. Rauch, M. Véron, Mater. Charact. 98 (2014) 1–9.
[26] B.S. El-Dasher, B.L. Adams, A.D. Rollett, Scr. Mater 48 (2003) 141–145.
[27] W. Pantleon, Scr. Mater. 58 (2008) 994–997.
[28] P.S. Bate, R.D. Knutsen, I. Brough, F.J. Humphreys, J. Microsc. 220 (2005) 36–46.
[29] S. Villert, C. Maurice, C. Wyon, R. Fortunier, J. Microsc. 233 (2009) 290–301.
[30] A.J. Wilkinson, G. Meaden, D.J. Dingley, Mater. Sci. Technol. 22 (2006) 1271–1278.
[31] T. Vermeij, J.P.M. Hoefnagels, Ultramicroscopy 191 (2018) 44–50.
[32] T.J. Ruggles, G.F. Bomarito, R.L. Qiu, J.D. Hochhalter, Ultramicroscopy 195 (2018) 85–92.
[33] Q. Shi, S. Roux, F. Latourte, F. Hild, Ultramicroscopy 199 (2019) 16–33.
[34] C. Zhu, K. Kaufmann, K.S. Vecchio, Ultramicroscopy 208 (2020) 112851.
[35] C. Ernould, B. Beausir, J.-.J. Fundenberger, V. Taupin, E. Bouzy, Acta Mater. (2020) in press, doi:10.1016/j.actamat.2020.03.026.
[36] T. Tanaka, A.J. Wilkinson, Ultramicroscopy 202 (2019) 87–99.
[37] T. Vermeij, M. De Graef, J. Hoefnagels, Scr. Mater. 162 (2019) 266–271.
[38] H. Yu, J. Liu, P. Karamched, A.J. Wilkinson, F. Hofmann, Scr. Mater. 164 (2019) 36–41.
[39] A.J. Wilkinson, D. Randman, Philos. Mag. 90 (2010) 1159–1177.
[40] J. Jiang, T.B. Britton, A.J. Wilkinson, Int. J. Plast. 69 (2015) 102–117.
[41] J.F. Nye, Acta Metall. 1 (1953) 153–162.
[42] B. Beausir, J.-.J. Fundengerger, Analysis Tools for Electron and X-Ray Diffraction, ATEX - Software, Université de Lorraine, Metz, 2017.
[43] R.G. Mariano, A. Yau, J.T. McKeown, M. Kumar, M.W. Kanan, ACS Omega 5 (2020) 2791–2799.
[44] A.C. Leff, C.R. Weinberger, M.L. Taheri, Ultramicroscopy 153 (2015) 9–21.